Research Article
Vol. 27, No. 17 | 19 Aug 2019 | OPTICS EXPRESS 23849
Optics EXPRESS

Metre-per-second microfluidic flow velocimetry with dual beam optical coherence tomography

Evangelos Rigas, Jonathan M. Hallam, Thomas O. H. Charrett, Helen D. Ford, and Ralph P. Tatam*

Centre for Engineering Photonics, Cranfield University, Cranfield, MK43 0AL, UK
**r.p.tatam@cranfield.ac.uk*

Abstract: A novel dual beam Optical Coherence Tomography (OCT) instrument has been developed for high velocity flow measurement, principally in microfluidics applications. The scanned dual beam approach creates a pair of image-frames separated by a small spatiotemporal offset. Metre-per-second flow measurement is achieved by rapid re-imaging by the second beam allowing for particle tracking between each image-frame of the pair. Flow at 1.06 m/s using a single optical access port has been measured, more than two orders of magnitude larger than previously reported OCT systems, at centimetre depth and with millimetre scale depth of field within a microfluidic chip, whilst simultaneously imaging the microfluidic channel structure.

Published by The Optical Society under the terms of the Creative Commons Attribution 4.0 License. Further distribution of this work must maintain attribution to the author(s) and the published article's title, journal citation, and DOI.

1. Introduction

Microfluidics is an increasingly significant research area, recognised as a key enabling technology across a broad range of applications [1,2]. There is therefore an increasing need for robust and straightforward imaging tools [2,3], for live monitoring during industrial or scientific bio-processes [4], to observe experiments in a research environment [5] and for characterise flows during the prototyping and development of new microfluidic chip designs [6].

Efforts have been made to integrate flow rate sensors into microfluidic chips either using intrusive sensors such as cantilevers which interfere with the flow, or non-invasive sensors measuring only at the edge the microfluidic channel [7]. In some cases optical waveguides have been integrated onto the microfluidic chip to provide an optical measurement [8], but this approach heavily restricts the design of the chip. On-chip sensors of any type typically provide flow measurement at only a single fixed location within the chip, as opposed to imaging techniques which can be used flexibly at any location within any chip.

The most commonly used optical microfluidic flow-measurement technique is 2-dimensional, 2-component (2D-2C) microscopic Particle Imaging Velocimetry (μPIV) [2,9] using standard microscopes. 2D-2C techniques capture an in-focus horizontal image of a flow seeded with fluorescent particles, and hence 2-component velocity information. Combined with high speed double-exposure camera technology, flows at metre-per-second velocities can be measured [9]. However, the technique suffers from the presence of out-of-focus light, compromising the image [2].

2-dimensional 3-component (2D-3C) stereoscopic measurements have been undertaken by combining images from two microscopes separated by a small angle. The resulting 3-component velocity information is from a thin 2-dimensional plane, and has poor velocity sensitivity due to the limited angle of separation between the microscope viewpoints; however, metre-per-second velocities can be achieved [2].

#364208 https://doi.org/10.1364/OE.27.023849
Journal © 2019 Received 3 Apr 2019; revised 20 May 2019; accepted 21 May 2019; published 6 Aug 2019

Optics EXPRESS

Confocal microscopy eliminates the out-of-focus light, at the cost of limiting the acquisition rate (and therefore the measurable velocity) [2,9]. Deployed as a 2D-2C technique flow velocities of 8 mm/s have been reported [3]. Alternatively, 3-dimensional 3-component (3D-3C) velocity information can be captured using confocal microscopy by recording multiple horizontal sections at different vertical depths in order to image a volume, then re-measuring that volume in order to track particles between the volumes; however, achievable volume imaging rates of around 30 Hz limit the technique to velocities slower than approximately 100 µm/s [10].

Truly 3-dimensional 3-component (3D-3C) microfluidic-velocimetry techniques such as Tomographic µPIV and micro-3-dimensional Particle Tracking Velocimetry (µ3D-PTV) [7,11] has been demonstrated, which can in principle measure 3-component velocity information in 3-dimensions at metre-per-second velocities. However, these techniques suffer from a number of limitations: they require optical access ports on multiple axis surrounding the microfluidic chip [9,11]; the measured velocities are difficult to calibrate [2,11]; and it can be difficult to locate the velocity measurement within the microfluidic chip as they cannot simultaneously image the flow and the structure of the microfluidic channel [12].

Holographic µPIV, and notably digital in-line holography [13], allows for reconstruction of the 3-dimensional 3-component flow velocity from only two optical access ports (above and below the microfluidic chip, on a single axis). This is achieved by reconstructing the intensity and phase information of the light scattered by the sample. Flow velocities of 3 mm/s along a curved microchannel have been measured using this technique [14].

Optical Coherence Tomography (OCT), a form of interferometry that creates depth-sectioned images [11] (including for dynamic situations [16]) is therefore an attractive complimentary technique for microfluidic flow measurement. OCT offers a convenient instrument potentially capable of acquiring 3D-3C velocity and channel structure information whilst requiring only a single optical access port. OCT is capable of imaging at centimetre depth within a microfluidic chip, across a millimetre-scale depth-of-field, and (due to the high signal-to-noise ratio of interferometric techniques) does not require fluorescent particles as commonly used in µPIV [17,18].

In modern swept-source OCT the laser wavelength is scanned over a bandwidth of approximately 100 nm, giving a z-axis (depth) resolution of micrometres, at a repetition frequency of kilohertz [19]. This creates a depth section of the sample at a single point (an A-scan, analogous to an ice core), with the horizontal (x-or-y-axis) resolution given by the diameter of the beam waist (typically a few micrometres) through an axial depth-of-field (typically a few millimetres) [11]. The laser beam is scanned horizontally on the x-axis by a galvanometer-mounted mirror to create a depth-section image (a B-scan). This B-scan rate is limited either by the speed of the galvanometer, or the sweep rate of the laser multiplied by the number of A-scans within the B-scan [11]. Typical rates of tens of hertz are sufficient to measure millimetre-per-second flow velocities. OCT has a wide range of applications including in the microfluidic area for blood-flow monitoring [18] and for functional analysis of microfluidic devices [17].

Another technique, Doppler OCT, has been used to measure flow velocities up to 30 mm/s [20]. Doppler OCT is distinct from normal OCT in that the sensitivity has an angular dependence on viewing angle, so insofar as is possible the instrument must look along the axis of flow, a significant limitation when used with microfluidic channels.

Here we report on a novel dual beam OCT system that has been constructed to overcome the velocity limitation imposed on micro-fluidic measurements made using OCT by the achievable B-scan rate. This system operates in the normal OCT mode, not the Doppler mode.

2. Theory of scanned dual beam OCT

It is useful to examine the theory governing the use of a scanned, dual beam OCT system for flow measurement. The interaction of the beam scan velocity, the particle flow velocity, the

Optics EXPRESS

beam separation, and the length of the scan have important implications for the measurable flow velocities, the resolution of those velocities, and the spatial resolution with which velocity information is captured. Particle flow velocity will be considered for the main direction of flow along the length of the microfluidic channel, which is the 'streamwise' component of flow velocity. The 'spanwise' component of flow velocity will be neglected.

The approach of creating a pair of image-frames with a scanned dual beam OCT system is outlined in Fig. 1(a). The first image-frame of the pair is created by Beam A and the second image-frame of the pair (separated by a small spatiotemporal delay) is created by Beam B. To measure a high velocity streamwise flow the two beams are scanned in the same plane (and hence the paired image-frames are also in that plane).

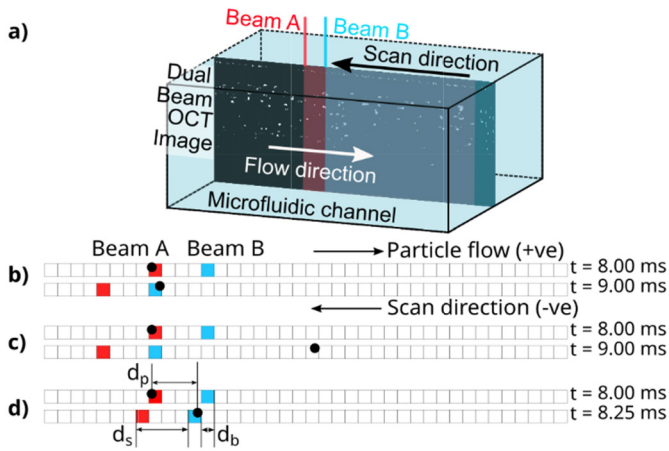

Fig. 1. (a) Principle of scanned dual beam OCT system, creating a pair of depth-sectional image-frames within the volume of a microfluidic channel. 1(b)-1(d) are theoretical cases of beam-particle interaction in a scanned dual beam system, described in the text. The 'spanwise' 2D depth-section has been collapsed to a 1D line, leaving only the 'streamwise' velocity. d_p is the distance moved by the particle between the paired image-frames, d_b is the distance moved by the beam scan in the same time, and d_s is the fixed separation between the beams.

Particles are tracked between each pair of image-frames, analogous to the approach taken in double-exposure camera PIV [9]. For stationary microfluidic channel structures or slow-moving particles (defined as having less than 10% of the beam scan velocity), the spatiotemporal delay between Beam A and Beam B is due to the velocity with which the beams are scanned and the physical separation between the beams.

The case is different for a particle with velocity faster than that of the beam scan, because the flow velocity determines not only the position of the particle in the two image-frames, but also the time separating the images of the particle within those frames. This is analogous to Laser-Two-Focus systems [21] where each focus acts as a 'gate'. OCT has the additional complexity of scanned beams. This can be clarified by considering the situations in Fig. 1(b)-1(d).

In the case of a slow-moving particle, Fig. 1(b), the particle is detected by Beam A at (for example) t = 8 ms, and has moved only a small distance when it is re-detected by Beam B at t = 9 ms. Thus, the distance that particle has moved, in the fixed time delay between the beams, is its velocity.

In the case of a fast-moving particle, Fig. 1(c), it is detected by Beam A at t = 8 ms; however, it is clear that it cannot be detected by Beam B at t = 9 ms because the particle has already passed this position. Instead, the particle is detected when it passes the position of Beam B, in this case, at t = 8.25 ms, Fig. 1(d).

Optics EXPRESS

This behaviour can be described with the following Eqs. (1)-(4). Taking time and position to be zero when the particle is first detected by Beam A, and defining the positive direction as being that of the particle flow (so that beam velocity v_b and distance moved by the beam d_b will take negative values). First, the distance-time-velocity Eq. (1) for the particle (p) and for scan of Beam B (b):

$$v_p = d_p / t, \tag{1a}$$

$$v_b = d_b / t. \tag{1b}$$

This implies that, Eq. (1b) rearranged for time t and substituted into Eq. (1a):

$$v_p = d_p v_b / d_b. \tag{2}$$

Together with this is the geometrical fact that the distance the particle has moved, d_p, when it is detected by Beam B can be related to the beam separation, d_s, by:

$$d_p = d_s + d_b. \tag{3}$$

This is the sum of the separation between the beams d_s and the distance moved d_b by Beam B. This then, Eq. (3) rearranged for d_b and substituted into Eq. (2), gives an expression for a detected particles velocity:

$$v_p = \frac{d_p v_b}{d_p - d_s}. \tag{4}$$

It is instructive to plot the determined particle velocity against the particle displacement that occurs between detection by Beam A and detection by Beam B, shown in Fig. 2. The beam scan moves in the negative 'x' direction and the particle velocity is expressed as a multiple of the scan velocity, for a beam separation of 55 times the diameter of the beam (b_x), provided consecutive A-scans do not overlap. This implies that the maximum particle displacement in the positive direction is 55.

Negative particle displacement (regime 1 in Fig. 2) implies that the particles are moving in the same direction as the beam scan. This results in improved velocity resolution; however, it is impossible to measure velocities that are greater than the beam scan speed, because in that case Beam B will never catch up with the particle following detection by Beam A (this asymptote can be seen along the graph at a particle velocity equal to the negative scan velocity). In practice, because the beam scan has a finite distance within which the second beam must catch up to the particle, the particle velocity must be substantially lower than the beam scan rate.

Optics EXPRESS

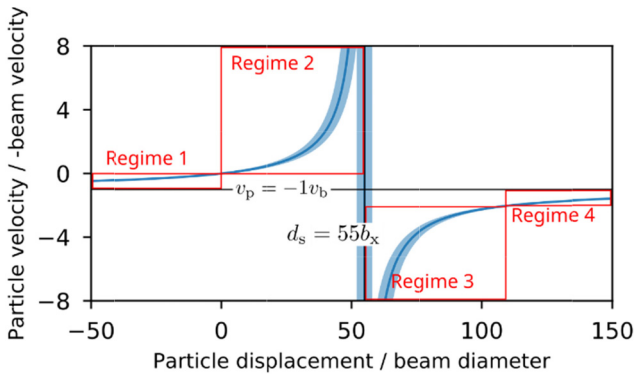

Fig. 2. Particle velocity v_p (as a multiple of negative scan velocity v_b), expressed as a function of the displacement of the particle between each image-frame of the pair d_p (as a multiple of the beam diameter) with a beam separation d_s of 55 times the beam diameter b_x. Hence both axis are dimensionless ratios between a measurement of the particle flow and a property of the instrument. Error band representing a 1-beam-diameter error in the determination of the particle displacement are shown.

Forward particle displacement between 0 and 55 (regime 2 in Fig. 2) represents motion towards the oncoming scanning beams. The determined velocity rises asymptotically as the particle displacement approaches the beam separation, and therefore so does the associated error bar. At the limiting case, where the particle is detected in the same acquisition sample (A-scan, or sweep of the laser wavelength) by both Beam A and Beam B, the particle displacement will be equal to the beam separation of 55 (as shown by the vertical line in Fig. 2). This means that no upper limit can be set on the particle velocity. Similar to the Laser-Two-Focus technique, the more widely separated the sensing beams are, the faster the velocity vectors that can be measured (and with more accurate resolution of the value of that velocity vector); however, the spatial resolution of the determined velocity vectors is compromised, this is not desirable because turbulent or re-circulatory regions cannot be identified. For extremely large beam separations it might not even be possible to match particles between the beams in which case velocimetry cannot be performed.

It is possible for a particle to move faster than the beam scan in the same direction as the beam scan (regimes 3 and 4 in Fig. 2). In this case, the particle is measured first by Beam B and then by Beam A, which appears in Fig. 2 as a discontinuity on the x-axis at a beam separation of 55 times the beam-diameter. In the case where the particle has a much greater velocity than the scan, this results in a large but poorly-resolved velocity (regime 3). As the velocity of the particle approaches that of the scan, the pixel displacement between detections increases because the particle is only slowly overtaking Beam A (regime 4).

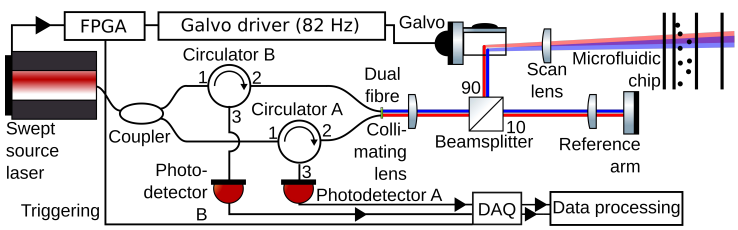

Fig. 3. Schematic of scanned dual beam OCT system. The laser output propagates to an optical-fibre coupler separating it into two OCT interferometers operating in parallel through the same set of bulk optic components. In free space Beam A is shown red and Beam B is shown blue, although their wavelengths are the same (colour online).

Optics EXPRESS

3. Methodology

A novel, prototype dual beam optical coherence tomography system was designed and built based on the foregoing analysis. The system was designed to set the beam scan direction opposite to the flow direction, falling entirely within regime 2 in Fig. 2. In this regime the number of pixels separating the particles between the Beam A image-frame and Beam B image-frame is minimised, which allows for more robust particle tracking. This imposes the cost of coarser velocity resolution, worsening logarithmically as the velocity increases (consistent with the theory outlined in Section 2). For this proof-of-concept, it was considered more important that the particle tracking be robust than to improve the velocity resolution.

Additionally, the spatial resolution of the streamwise velocities is equal to the number of pixels between the two detected particle positions d_p, and thus regime 2 also allows for higher spatial resolution of velocity vectors. Although spatially-resolved flow velocity vector results are not presented herein, it is anticipated that they will form an important use-case of the instrument in the future and hence the concept will be proven using regime 2. The schematic of the system is shown in Fig. 3. The microfluidic channel to be imaged is addressed using a bespoke dual optical fibre end, coupled through a compact OCT scan head. The values used for this system were: d_s of 56, with a beam separation of 180 µm, giving an effective b_x of 3.2 µm, although the actual beam diameter at focus is 10 µm (differing because there is some beam-overlap between adjacent A-scans). The scan velocity v_b was 147.6 mm/s.

3.1 Microfluidic channel, seed particles and pump

To track the flow, 10 µm diameter latex spheres were used as seeding particles. A colloidal suspension was prepared at a density of 1.05 g/ml, matched to the particles so they would remain in suspension and accurately follow the flow. The fluid was a mixture of partial buffer solution (PBS, 68% by volume), glycerol (27% by volume), and concentrated latex sphere solution (5% by volume, i.e. 0.5% latex spheres overall) with Tween20 (0.1% by volume) to prevent biofilm growth. The characteristic time of the particles was 2.28 µs [22].

The internal dimensions of the flow channel are 12.8 mm (‘streamwise’ or ‘length’) x 1.25 mm (‘width’) x 0.7 mm (‘spanwise’ or ‘depth’) with sloped input sections. With a hydraulic diameter of 897.4 µm and flow velocities up to 3 m/s the Reynolds number is at most 1104 and is below the laminar-to-turbulent transition. Additionally, the Stokes number for a flow velocity of 3 m/s is 0.00761, hence the tracer particles will accurately follow the flow at least up to that velocity [22]. Flexible tubing of internal diameter 0.78 mm and the minimal possible length is attached to 50 ml plastic syringes mounted in two push-pull syringe pumps.

3.2 Optical fibre OCT system

The OCT system is driven by an Akinetic Swept Source Laser [19] delivering 9 mW of power whilst sweeping the wavelength between 1526 nm and 1608 nm at a rate of 96 kHz. This light is immediately split by a broadband (1450-1650 nm) single-mode 50:50 coupler for the two beams, as in Fig. 3. The light for each beam propagates from port 1 to port 2 of a broadband (1525-1610 nm) circulator to the OCT scan head unit via the bespoke dual optical fibre end. Returning light from the OCT scan head unit is propagated from port 2 to port 3 of a circulator to a photodetector. Each beam uses its own circulator and photodetector (balanced detection is not used), and the image created by each beam is recorded separately. The circulators optimise the use of the available light, maximising the signal to noise ratio (SNR), whilst isolating the laser. The bandwidth is limited by a passive electronic filter to 60 MHz to reduce the photodetector noise.

3.3 Dual optical fibre end

The bespoke dual optical fibre end used is shown in Fig. 4(a). This was created by bonding two single-mode 1550 nm telecommunication optical fibres into a single ceramic ferrule. The

Optics EXPRESS

optical fibres had a 9 µm core diameter, 125 µm cladding diameter, and the ferrule had an internal diameter of 270 µm. The ferrule was then mounted in an FC/APC connector and angle-polished to eight degrees in the orientation shown in Fig. 4(c) so each optical fibre core would be the same distance from the collimating lens when mounted; hence, both beams can be collimated simultaneously. The separation distance between the optical fibre cores was imaged using an optical microscope and determined to be 125 ± 2 µm. An infrared camera without lenses was positioned as a sample in the OCT system. The spots from the 1526-1608 nm laser, as imaged onto the CMOS chip, are shown in Fig. 4(b).

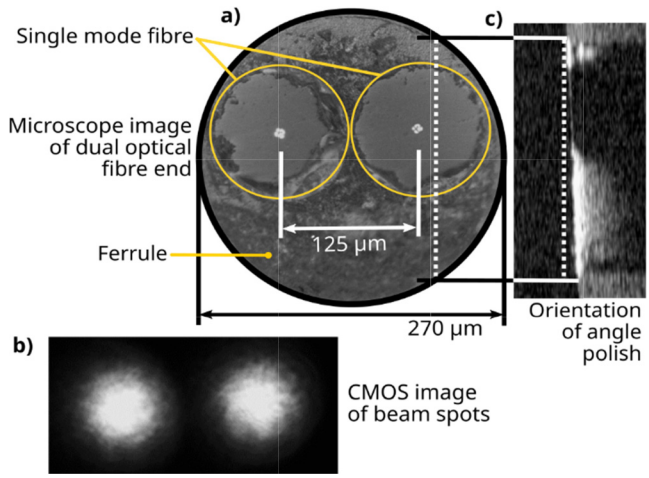

Fig. 4. (a) en-face microscope image of the bespoke dual optical fibre end, with the optical cores illuminated from the far end using a 560nm laser, resulting in multimode beam spots. 4(b) infrared CMOS-chip image of the beam spots from the OCT system using the 1526-1608 nm Insight laser. 4(c) OCT image of the optical fibre end showing the orientation of the angle polish. The optical fibre transmits the light and appears dark, the epoxy bonding agent scatters the light and appears bright.

3.4 OCT scan head

Light is coupled into the OCT scan head via the dual optical fibre end. The use of an FC/APC connector allows a robust and stable connection to be formed, mounted in a z-axis micrometre stage so the focal length to the collimating lens can be precisely set. The light is collimated by an achromatic doublet lens. A 1-inch diameter lens was chosen to minimise the effects of spherical aberration. The lens was mounted in a micrometre x-and-y stage, so the lens can be precisely centred between the two cores of the optical fibre end. The light then propagates through free space to a beamsplitter cube that reflects 90% of the incident optical power. The 10% of light transmitted is directed to a lens which focuses that light onto a flat reference mirror. Both the lens and non-reflective surfaces of the beamsplitter are broadband anti-reflection coated (1050-1700 nm).

The microfluidic channel is illuminated by the input light reflected by the beamsplitter (90%). x-and-y steering of the beams is accomplished by a silvered galvanometer mirror system. The beams are focused into the microfluidic channel using an OCT scan lens with 36 mm focal length. This represents a compromise [15] between narrow beam-waist for good lateral resolution, whilst still having sufficient depth-of-field to image a 700 µm deep microfluidic channel within a 1.5 mm thick microfluidic chip.

The lenses magnify the 125 ± 2 µm separation of the optical fibres to a 180 ± 3 µm beam separation at the microfluidic channel. This was measured by imaging the particles suspended within the microfluidic channel, with the pumping system deactivated. Consecutive Beam A image-frames (at 82 Hz, 12 ms apart) were used to identify particles which had not moved.

The beam separation was then determined using the paired Beam A, Beam B image-frames. A low particle density was used to minimise the possibility of confusion between particles. Of 16 stationary particles observed in the Beam A image-frames, 13 had unambiguous partners in the Beam B image-frame. The spacing between the known-to-be-stationary particles (and hence the beam spacing) was compared and identified to be 56 ± 1 pixels. Calibrating this to the full 560 pixel, 1.8mm length of the galvanometer scan gives a beam separation of 180 ± 3 μm.

3.5 OCT data capture and processing

The data is captured at 500 MS/s in 12-bit resolution using an ATS9350 DAQ. The initial data processing creates OCT images. The laser is electronically scanned, and mode-hops occur at particular times within the scan. A Data Valid Vector (DVV) corresponding to usable wavelengths is produced from an internal self-validation interferometer within the laser, and applied to the captured data to disregard data points subject to mode-hops [19]. It is generated prior to the measurement and is dependent on temperature, humidity and other conditions of the laboratory. A Blackman-Harris window is applied to the data to prevent ringing artefacts in the Fourier transform due to non-continuous signals [23]. Finally, a Fast Fourier Transform (FFT) is performed to obtain each A-scan, which are assembled to form an image-frame from each of Beam A and Beam B, at an 82 Hz refresh rate. These then form the input for the particle-identification and flow-tracking post-processing.

Bespoke data-acquisition and processing code allows direct recording of 4096 data points in each 96 kHz A-scan to a solid-state hard disk drive at a rate of 48 kHz for post-processing (i.e. every other A-scan is recorded). This is a limitation of the data acquisition hardware, and corresponds to a refresh rate of 82 Hz for a 600 pixel wide B-scan image (including 50 pixels of galvanometer flyback). Alternatively, live data processing can be achieved at 50 frames-per-second.

3.6 Particle identification and flow tracking

Particle identification and flow tracking was performed using the trackpy 0.3.2 library as outlined in Fig. 5 [24]. There are two processes: identifying the particle locations; and the particle linking that determines the flow velocity.

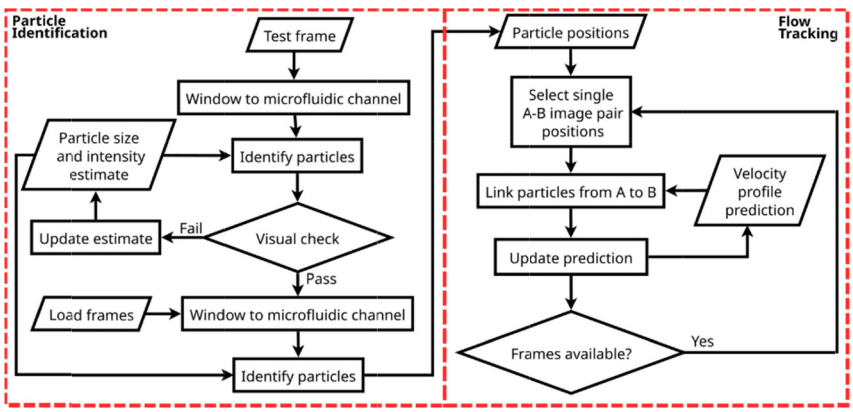

Fig. 5. Particle identification and flow tracking procedure using trackpy 0.3.2 library.

For the particle locations the image-frames are windowed to the microfluidic channel (using the capability of the instrument to simultaneously image the channel structure). Estimates for particle size and minimum separation are provided to provisionally locate the

particles. A visual check is performed on a test frame and if satisfactory the identification is repeated for all frames.

For the determination of flow velocity, the particle locations from a single A-B image-frame pair are linked using the trackpy library. The algorithm searches for a minimal matrix of velocity vectors that link particle positions between the A-B image-frame pair shown in Fig. 7(c). The search starts from an initial predictor for channel flow which anticipates particles moving primarily in the streamwise direction.

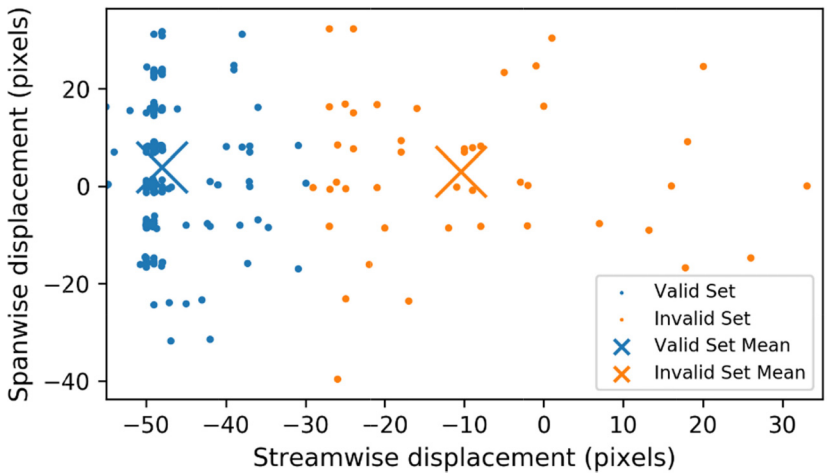

Fig. 6. K-mean filtering used to separate valid and invalid sets of particle trajectories. Particles are binned in spanwise, streamwise and in time. The chosen example bin is at the middle of the channel.

For the flow velocities profile shown in Fig. 7 the velocities were determined along the channel throughout the duration of a 3.6 second measurement. Following standard PIV methods [9] the velocity vectors were binned both spanwise and streamwise through the channel. It was observed that the velocities calculated by the particle tracking algorithm for each bin had two distinct clusters in velocity space, as shown in Fig. 6, one cluster representing the true velocities calculated from correctly-matched particles, and a second cluster, around zero velocity, corresponding to mis-matched particle pairs, where the algorithm attempts to minimise the particle translation in determining the match. K-mean filtering [25] was used to separate these clusters, and outlier velocities greater than 0.8 standard deviations from the mean were discarded. Approximately 60% of identified particles were plausibly matched to a particle in the paired frame. This is likely due to particles moving out of plane, implying cross-velocity components in the range of 1/18th the streamwise velocity (since the beams are separated by 180 μm and have width 10 μm). For the velocity profile over time shown in Fig. 8, K-mean filtering was not performed (since before the pump system is activated there is only a single cluster at zero).

4. Results from dual beam OCT system velocimetry

4.1 OCT images

OCT images from the dual beam instrument are shown in Fig. 7(b), and a schematic of the microfluidic chip Fig. 7(a). The identified particles are shown in Fig. 7(c) and the particle tracking velocity vectors are shown in Fig. 7(d). As an interferometric measurement OCT detects interfaces between regions of different refractive index [15]. The interface between the lid of the microfluidic chip and the air creates a strong signal, appearing as a dark line at the top of both the image from Beam A (outlined red) and Beam B (outlined blue, colour online). The upper interface between the material of the microfluidic chip and the fluid within the

microfluidic channel can be seen at 140 µm depth, and 700 µm beneath is the lower surface of the microfluidic channel. This gives a simultaneous image of the microfluidic channel structure alongside the microfluidic flow measurement which was used to position the flow measurement in a straight section of the channel and to insure the channel was level.

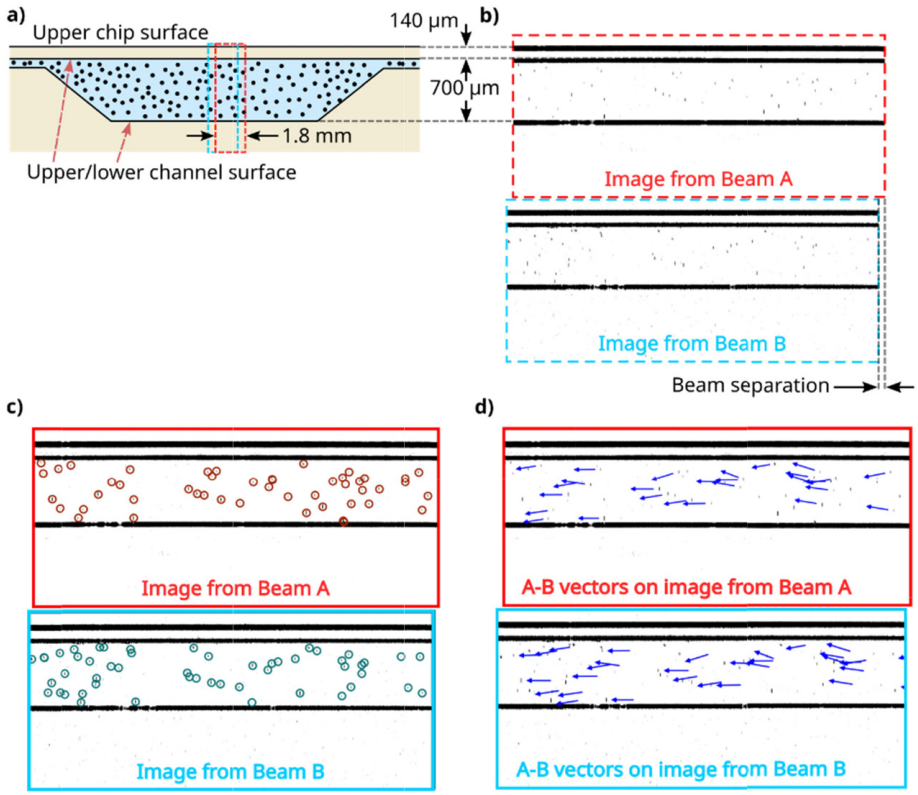

Fig. 7. (a) Microfluidic channel schematic, (b) Beam A image-frame and Beam B image-frame, (c) with particle identification, (d) with flow tracking vectors. The OCT images have been colour-inverted for display.

Within the microfluidic channel images, Fig. 7(b), the 10 µm particles appear as dark spots. Since these particles are of similar scale to the depth resolution, the interface between the top of the particle and the fluid, and the interface between the bottom of the particle and the fluid, are merged and each particle appears as a single point. Some particles appear less intensely than others, likely because they lie only partially within the plane of the dual beam scan. Note that the particles near the centre of the microfluidic channel appear compressed compared to those near the upper and lower surfaces. This is because (since the microfluidic channel experiences parabolic flow) these particles have faster flow velocities than those near the edges, therefore, they pass more swiftly through the scanning OCT beams creating the images, and thus have a narrower length ('streamwise') profile. Their depth ('spanwise') profile is unaffected. A traditional camera-based system would experience this effect as 'streaking' in the streamwise direction.

The particle density used in the measurement can be seen in Fig. 7. The use of the trackpy particle tracking velocimetry software imposes a relatively sparse particle density, since the software is searching for a unique matrix of velocity vectors connecting particle positions between the A image-frame and the B image-frame. If the particle density were high, many

Optics EXPRESS

possible matrix (corresponding to particle mismatches) would exist. It is important to note that this is a limitation of the tracking technique chosen and the images from the dual-beam OCT instrumentation is compatible with PIV techniques which allow substantially higher particle densities. For this proof-of-principle work it was decided that the methodological clarity offered by unique particle tracking was preferable to using PIV.

Further, the representative images used in Fig. 7 represent a peak flow rate of approximately 0.5 m/s. The images shown in Fig. 7 are captured in 1/82nd of a second, and have a length of 1.8 mm. All particles passing through that length in that time appear in the image. Therefore the number of particles appearing in the image – the apparent particle density – depends upon the flow velocity. At the peak flow velocity of 1 m/s the number of particles present in an image is approximately double that shown in Fig. 7. Of course the number of particles present per volume of fluid remains fixed – but a greater volume of fluid passes through the image during the capture when the fluid is moving faster. The particle density was not precisely tuned to a particular flow velocity, but was appropriate for measuring flows in the millimetre-to-metre-per-second regime. A higher particle density would be required to measure micrometre-to-millimetre-per-second flow velocities.

4.2 Flow velocity profile

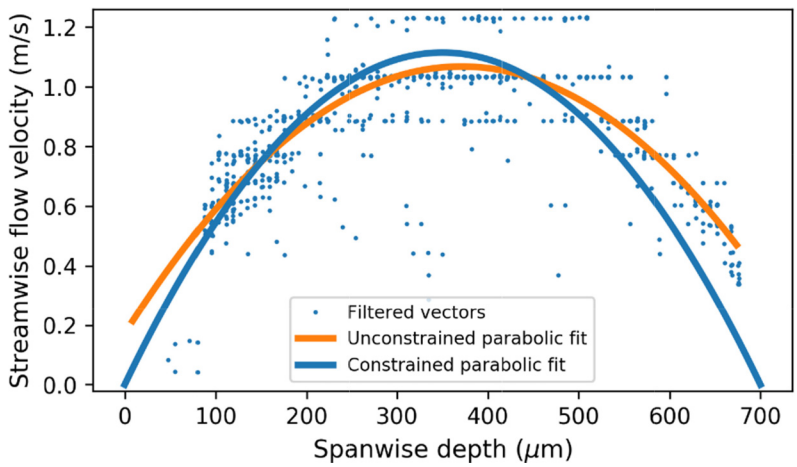

Fig. 8. Individual velocity vectors, unconstrained parabolic fit, and constrained parabolic fit from t = 0 sec to t = 3.6 sec, taken at 0.61 mm width (the middle of the channel).

The streamwise component of the determined velocity vectors identified for a single image-frame pair in Fig. 7(d) is shown in Fig. 8. This measurement was performed over a 3.6 second period in the central position (0.61 mm) across the channel. The degree of velocity spread shown in Fig. 8 is due both to velocity digitization of the instrument, and small variations in the flow rate during the measurement due to syringe pump pulsation.

It can be seen that there is some degree of digitization on the y-axis, which is due to pixel-locking [9]. As the particle velocity increases the particles increasingly interact with the beams for only a single A-scan, meaning their streamwise position can only be determined to be somewhere within that single pixel. This pixel-locking has a logarithmic effect in terms of velocity digitization due to the non-linearity shown in Fig. 2. Since there is digitization of two particle positions, the separation of which corresponds to the velocity, there are three possible determined velocities for each pair of digitised particle positions. These digitized levels are at velocity values of 1.23 m/s, 1.03 m/s, 0.89 m/s and 0.77 m/s. As measured velocity continues to fall, sufficient particles appear across multiple pixels (with the determined position set by the relative intensity of those pixels) that digitisation becomes relatively minor below 0.77 m/s. This effect is also why the digitization is not complete, even at 1.23 m/s.

Optics EXPRESS

The microfluidic flow velocity must fall to zero at the edges of the channel due to the no-slip condition [22]. Given the dimensions of the microfluidic channel (0.7 mm x 1.25 mm), parabolic flow is to be expected far from the inlet [22,26]. A parabolic fit constrained to zero at the edges of the microfluidic channel, ensures this condition is met smoothly by the velocity profile. The peak velocity value of the constrained parabolic fit is 1.11 ± 0.02 m/s. This measurement was repeated at eight different positions across the channel, allowing a volume flow rate to be calculated by integrating the area beneath the fitted velocity curve. The constrained fit implies a flow rate of 31.0 ± 0.4 mL/min, compared to the syringe pump setting of 32.8 ± 0.5 mL/min (with the uncertainty set by variation in the internal diameter of the syringe).

The channel has length 12.8 mm with sloped input sections of length 0.9 mm at either end. Although the measurement was performed in the middle of the channel it is plausible that the 'far from the inlet' condition is not fully met, and that this particular flow is better modelled across the middle of the channel by an unconstrained fit extending to within 30 micrometres (3 particle widths) of the edge of the channel, with the velocity then falling rapidly to zero at the edge of the channel. This unconstrained fit was also performed giving a peak velocity of 1.06 ± 0.02 m/s and an implied flow volume of 32.7 ± 0.4 mL/min that is closer to the expected value. This fit appears to skew the flow velocity in favour of the deeper sections of the channel, which may be due to the sloped input sections of the microfluidic channel, particularly at such high velocities which imply that the median particle travels the entire 12.8 mm length of the channel in approximately 20 milliseconds.

4.3 Time-resolved flow velocity profile

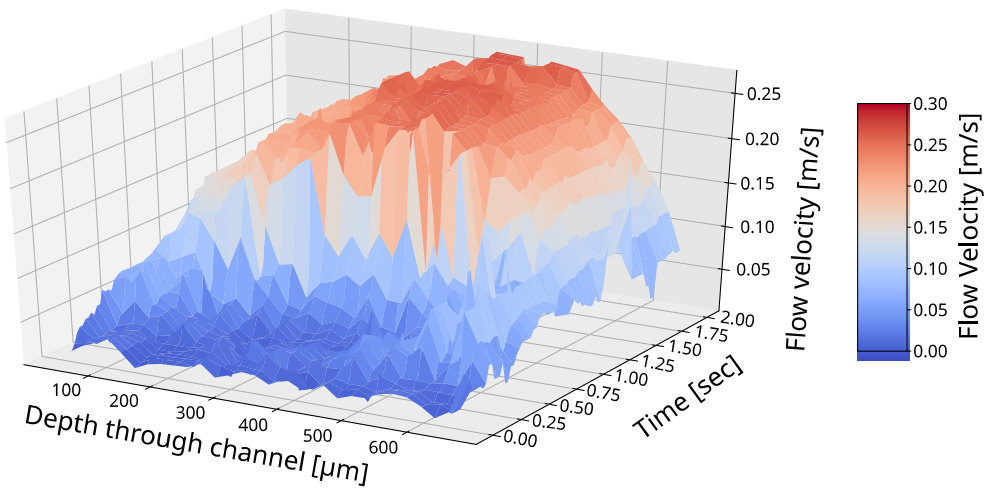

Fig. 9. Evolution of the flow velocity over time as determined using the dual beam OCT system and particle tracking approach. Here the average flow velocity computed over a rolling 20 frame period is shown for each of 30 spanwise depth bins to determine the streamwise flow velocity.

In many circumstances it will be desirable to monitor changes in the flow over time. The determined particle velocities were analysed by computing the average velocity vector using a rolling 20 frame period (0.25 seconds) in each of 30 bins of equal width across the channel, and the velocity profile over time is shown in Fig. 9. Here the start-up of the pump at approximately t = 0 to 1 second can clearly be seen, together with the steady state parabolic flow, t ≥ 1 second.

5. Discussion and conclusions

A novel dual beam OCT system has been constructed to overcome the typical B-scan rate limitation on velocities measurable by OCT systems. This dual-beam instrument creates a pair

of image-frames separated by a small spatiotemporal offset. Metre-per-second measurement is achieved because the rapid re-imaging by the second beam allows for particle tracking between each image-frame of the pair. We have demonstrated measurements of microchannel flow with peak velocities of 1.06 m/s (along with simultaneous imaging of the microfluidic channel structure which was used to position the flow velocity measurement and ensure the channel was level). The flow rate setting of the pump (32.8 ± 0.5 mL/min) is in agreement with the measured flow rate (32.7 ± 0.4 mL/min) for an unconstrained parabolic fit.

There are a number of limitations to this dual-beam OCT instrument. At these high velocities, the system suffers from logarithmic coarsening of the velocity resolution, representing a significant disadvantage compared to other high velocity techniques. This can be resolved by wider spacing of the optical fibre cores in the bespoke dual optical fibre end; however, that would further separate the A and B image-frames increasing the difficulty of particle tracking. Increasing the number of optical fibre cores will allow widely separated measurements with fine velocity resolution and acceptable particle tracking to be made because the particles can be tracked from core to core. Alternatively, increasing the laser sweep rate will allow faster A-scans leading to smaller pixels in the streamwise direction and hence enhanced velocity resolution.

In the current configuration of the instrument, the flow can only be measured so long as the particles remain in the plane of the beam scan. This means out-of-plane velocity components must be less than 1/18th the streamwise velocity component (since the spacing between the beams is 18 times the beam width). The magnitude of the allowed out-of-plane velocity component can be increased by reducing the spacing of the dual optical fibre end; however, this further coarsens the velocity resolution. Increasing the number of optical fibre cores aligned with the beam scan again offers a solution. Alternatively, adding a second pair of optical fibre cores alongside the first might allow out-of-plane velocity components to be tracked between the two pairs.

It is desirable, but not required, for the interaction of the particle flow velocity and the beam scan direction to fall within regime 2 shown in Fig. 2. Flow in the same direction as the beam scan – which may not be possible to avoid, for example in the case of re-circulatory regions - can still be detected, but the particle tracking software would require modification to correctly interpret the flow velocities in regimes other than 2.

In the described scanning mode the spatial resolution of velocity vectors may be limited by the low particle density required by the use of trackpy particle tracking velocimetry software. The images generated by the dual-beam OCT instrument are compatible with PIV techniques that would support higher particle densities for better spatially-resolved flow velocity vector measurements.

In comparison to other techniques, the measured (depth-section) streamwise velocities are over two orders of magnitude higher than previously reported (depth-section) OCT flow measurements [17,18] and (horizontal-section) confocal microscopy measurements [3,9]. In common with (some implementations) of these techniques, dual-beam OCT requires only a single optical access port (from above or below the microfluidic chip on a single axis), allowing for a convenient measurement. Although (horizontal-section) 2D-2C µPIV can measure equivalent flow velocities, it cannot reject out of focus light, whereas dual-beam OCT can. Tomographic µPIV requires multiple viewing ports on multiple optical axis whilst dual-beam OCT does not. Digital in-line holography only requires a single optical axis but both optical ports on that axis (above and below the microfluidic chip) must be accessible.

This system could be used in alternative scanning modes, such as capturing 3-dimensional 3-component velocity information between a pair of ‘gates’ scanned across the ‘streamwise’ direction of flow, a measurement which would be impossible at any velocity using a traditional OCT system. Alternatively, it would be possible to capture 2-dimensional high-velocity flows through a volume (albeit at different times within that volume) by translating the technique presented herein through that volume.

Optics EXPRESS

Funding

Engineering and Physical Sciences Research Council (EPSRC), UK, (EP/L014637/1, EP/H02252X/1, and EP/N002520/1).

Acknowledgements

We acknowledge the support of our colleague Dr M Partridge in creating the microparticle mixture. We dedicate this work to our colleague Dr Helen D Ford (1963–2018). The underlying data can be accessed through the Cranfield University data repository at 10.17862/cranfield.rd.7628933

Disclosures

The authors declare that there are no conflicts of interest related to this article.

References

1. G. M. Whitesides, "The origins and the future of microfluidics," Nature **442**(7101), 368–373 (2006).
2. R. Lindken, M. Rossi, S. Grosse, and J. Westerweel, "Micro-Particle Image Velocimetry (microPIV): recent developments, applications, and guidelines," Lab Chip **9**(17), 2551–2567 (2009).
3. A. M. C. van Dinther, C. G. P. H. Schroën, F. J. Vergeldt, R. G. M. van der Sman, and R. M. Boom, "Suspension flow in microfluidic devices--a review of experimental techniques focussing on concentration and velocity gradients," Adv. Colloid Interface Sci. **173**, 23–34 (2012).
4. M. Karle, S. K. Vashist, R. Zengerle, and F. von Stetten, "Microfluidic solutions enabling continuous processing and monitoring of biological samples: A review," Anal. Chim. Acta **929**, 1–22 (2016).
5. D. Bento, R. O. Rodrigues, V. Faustino, D. Pinho, C. S. Fernandes, A. I. Pereira, V. Garcia, J. M. Miranda, and R. Lima, "Deformation of red blood cells, air bubbles, and droplets in microfluidic devices: Flow visualizations and measurements," Micromachines (Basel) **9**(4), 151 (2018).
6. R. Amin, S. Knowlton, A. Hart, B. Yenilmez, F. Ghaderinezhad, S. Katebifar, M. Messina, A. Khademhosseini, and S. Tasoglu, "3D-printed microfluidic devices," Biofabrication **8**(2), 022001 (2016).
7. M. H. Zarifi, H. Sadabadi, S. H. Hejazi, M. Daneshmand, and A. Sanati-Nezhad, "Noncontact and nonintrusive microwave-microfluidic flow sensor for energy and biomedical engineering," Sci. Rep. **8**(1), 139 (2018).
8. S. M. Azmayesh-Fard and R. G. DeCorby, "Lab on a chip for measurement of particulate flow velocity using a single detector," Meas. Sci. Technol. **29**(9), 095013 (2018).
9. M. Raffel, C. E. Willert, and J. Kompenhans, *Particle Image Velocimetry - A Practical Guide* (Springer, 2007).
10. A. Klein, J. L. Moran, D. H. Frakes, and J. D. Posner, "Three-dimensional three-component particle velocimetry for microscale flows using volumetric scanning," Meas. Sci. Technol. **23**(8), 085304 (2012).
11. H. Kim, J. Westerweel, and G. E. Elsinga, "Comparison of tomo-PIV and 3D-PTV for microfluidic flows," Meas. Sci. Technol. **24**(2), 024007 (2013).
12. C. Cierpka and C. J. Kähler, "Particle imaging techniques for volumetric three-component (3D3C) velocity measurements in microfluidics," J. Vis. (Tokyo) **15**(1), 1–31 (2012).
13. J. Wu, G. Zheng, and L. M. Lee, "Optical imaging techniques in microfluidics and their applications," Lab Chip **12**(19), 3566–3575 (2012).
14. X.-B. Li, M. Oishi, T. Matsuo, M. Oshima, and F.-C. Li, "Measurement of viscoelastic fluid flow in the curved microchannel using digital holographic microscope and polarized camera," J. Fluids Eng. **138**(9), 091401 (2016).
15. J. A. Izatt, M. A. Choma, and A.-H. Dalla, "Theory of optical coherence tomography," in *Optical Coherence Tomography*, W. Drexler and J. G. Fujimoto, eds. (Springer International Publishing, 2015), 2nd ed, vol. 1.
16. H. D. Ford and R. P. Tatam, "Spatially-resolved volume monitoring of adhesive cure using correlated-image optical coherence tomography," Int. J. Adhes. Adhes. **42**, 21–29 (2013).
17. B. Dong, S. Chen, F. Zhou, C. H. Y. Chan, J. Yi, H. F. Zhang, and C. Sun, "Real-time functional analysis of inertial microfluidic devices via spectral domain optical coherence tomography," Sci. Rep. **6**(1), 33250 (2016).
18. R. K. Wang, Q. Zhang, Y. Li, and S. Song, "Optical coherence tomography angiography-based capillary velocimetry," J. Biomed. Opt. **22**(6), 66008 (2017).
19. M. P. Minneman, J. Ensher, M. Crawford, and D. Derickson, "All-semiconductor high-speed akinetic swept-source for OCT," Proc. SPIE **8311**, 831116 (2011).
20. J. Lauri, J. Czajkowski, R. Myllylä, and T. Fabritius, "Measuring flow dynamics in a microfluidic chip using optical coherence tomography with 1 µm axial resolution," Flow Meas. Instrum. **43**, 1–5 (2015).
21. T. O. H. Charrett, S. W. James, and R. P. Tatam, "Optical fibre laser velocimetry: A review," Meas. Sci. Technol. **23**(3), 032001 (2012).
22. C. Tropea, A. Yarin, and J. F. Foss, *Springer Handbook of Experimental Fluid Mechanics* (Springer, 2007).
23. F. Zhang, Z. Geng, and W. Yuan, "The algorithm of interpolating windowed FFT for harmonic analysis of electric power system," IEEE Trans. Power Deliv. **16**(2), 160–164 (2001).

Optics EXPRESS

24. D. Allan, T. Caswell, N. Keim, and C. van der Wel, trackpy: Trackpy v0.3.2 (2016). https://soft-matter.github.io/trackpy/v0.3.2/.
25. D. T. Larose, *Discovering Knowledge in Data: An Introduction to Data Mining* (Wiley-Interscience, 2005).
26. Y. A. Cengel and J. M. Cimbala, *Fluid Mechanics: Fundamentals and Applications* (McGraw-Hill, 2006).

138.250.27.251 {ts '2019-11-15 09:46:10'}

https://dspace.org/

Metre-per-second microfluidic flow velocimetry with dual beam optical coherence tomography

Rigas, Evangelos; Hallam, Jonathan M.; Charrett, Thomas O. H.; Ford, H. D.; Tatam, Ralph P.

2019-08-19
Optical Society of America
https://doi.org/10.1364/OE.27.023849
Rigas E, Hallam JM, Charrett TOH, et al., (2019) Metre-per-second microfluidic flow velocimetry with dual beam optical coherence tomography. Optics Express, Volume 27, Issue 17, 2019, pp. 23849-23863

Downloaded from a DSpace repository. https://dspace.org/